

Article

# Thermal Conduction Simulation Based on Reconstructed Digital Rocks with Respect to Fractures

Haiyuan Yang <sup>1</sup>, Li Zhang <sup>2</sup>, Ronghe Liu <sup>2</sup>, Xianli Wen <sup>3</sup>, Yongfei Yang <sup>1,\*</sup> , Lei Zhang <sup>1</sup>, Kai Zhang <sup>1</sup> and Roohollah Askari <sup>4</sup> 

<sup>1</sup> Key Laboratory of Unconventional Oil & Gas Development (China University of Petroleum (East China)), Ministry of Education, Qingdao 266580, P.R. China & Research Center of Multiphase Flow in Porous Media, School of Petroleum Engineering, China University of Petroleum (East China), Qingdao 266580, China

<sup>2</sup> Geological Exploration & Development Research Institute, CNPC Chuanqing Drilling Engineering Company Limited, Chengdu 610051, China

<sup>3</sup> Engineering Technology Research Institute of Xinjiang Oilfield Company, Wulumuqi 834000, China

<sup>4</sup> Department of Geological and Mining Engineering and Sciences, Michigan Technological University, Houghton, MI 49931, USA

\* Correspondence: yangyongfei@upc.edu.cn

Received: 27 May 2019; Accepted: 8 July 2019; Published: 18 July 2019



**Abstract:** Effective thermal conductivity (ETC), as a necessary parameter in the thermal properties of rock, is affected by the pore structure and the thermal conduction conditions. To evaluate the effect of fractures and saturated fluids on sandstone's thermal conductivity, we simulated thermal conduction along three orthogonal (*X*, *Y*, and *Z*) directions under air- and water-saturated conditions on reconstructed digital rocks with different fractures. The results show that the temperature distribution is separated by the fracture. The significant difference between the thermal conductivities of solid and fluid is the primary factor influencing the temperature distribution, and the thermal conduction mainly depends on the solid phase. A nonlinear reduction of ETC is observed with increasing fracture length and angle. Only when the values of the fracture length and angle are large, a negative effect of fracture aperture on the ETC is apparent. Based on the partial least squares (PLS) regression method, the fluid thermal conductivity shows the greatest positive influence on the ETC value. The fracture length and angle are two other factors significantly influencing the ETC, while the impact of fracture aperture may be ignored. We obtained a predictive equation of ETC which considers the related parameters of digital rocks, including the fracture length, fracture aperture, angle between the fracture and the heat flux direction, porosity, and the thermal conductivity of saturated fluid.

**Keywords:** digital rock; effective thermal conductivity; fracture; sandstone; thermal conduction simulation

## 1. Introduction

The thermal properties and temperature-dependent petrophysical properties of rock, such as heat capacity, thermal conductivity, compressive strength, permeability, and porosity, are of great importance in many fields of applied geosciences. For instance, the heat capacity of water and the thermal conductivity of geothermal reservoir affect the thermal production directly [1–4]. Rock permeability, which depends on temperature, is a key parameter in the underground storage of radioactive nuclear waste [5,6]. Thermal oil recovery can increase the hydraulic conductivity of heavy oil, thus improve the oil production [7,8].

The effective thermal conductivity (ETC) is an essential parameter to evaluate rock thermal conduction during the operation of geological engineering. Many experimental, numerical, and

analytical studies have been conducted to evaluate different factors that affect thermal conduction, the leading factor of which is the rock structure (size, shape, and distribution of pores). Huai et al. [9] reported that the spatial distribution of large pores had a substantive influence on ETC in fractal porous media. Pia et al. [10] studied the effect of the pore size, geometric organization, and complexity of porous media on the ETC. For fractured porous media, Miao et al. [11] derived the analytical solution of the axial effective thermal conductivities of fractal porous media by considering porosities, fractal dimensions, tortuosity fractal dimension, and fracture orientation effects. In addition to the pore structure, the conditions of thermal conduction, such as temperature, pressure, and saturating fluids, also affect ETC. The effect of temperature and pressure on rock ETC can be attributed to the variation of pore structure [12–15]. Different kinds of fluid filled in the pore space and various saturation of fluid also affect the thermal conduction ability of rock [16–18].

Many models have been developed to predict ETC of porous media [19,20], however, for a given sample, various ETC values can be obtained with respect to the heat flux directions, especially in samples with fractures. Zhou et al. [21] found that the fracture direction had a significant anisotropic effect on axial and lateral ETC. Besides, directional development of the contact area and pore structure under anisotropic stress conditions resulted in anisotropy of the thermal conductivity [22]. Askari et al. [23] reported that granular media with rough grains exhibited apparent anisotropy in the ratio of the directional thermal conductivities.

Digital rock as an advanced technology has been widely used in experiments and simulations of porous media due to its digitalization and visualization advantages [24–26]. For instance, using X-ray computed tomography, the real characterization of pore structures can be described accurately [27–29]. To solve the difficulty of experiments on tight rocks, the hydraulic conductivity can be calculated based on digital rocks that are constructed from real rocks [30–33]. Using the reservoir static properties obtained from digital rocks, automated fitting methods can predict the dynamic reservoir properties [34,35]. Although flow properties have been widely evaluated, thermal properties based on digital rocks are seldom studied [36–38].

As a kind of common sedimentary rock, sandstone exists extensively in geological settings. Therefore, characterizing the thermal properties of sandstone digital rocks is essential to optimize the production of fossil fuel and geothermal energy from underground formations [39,40]. Meanwhile, due to anisotropy, the heat flux direction must be considered when studying the ETC of sandstone [14,41]. The effective evaluation of the influencing factors of ETC is still needed. In this paper, we carried out thermal conduction simulations along three orthogonal ( $X$ ,  $Y$ , and  $Z$ ) directions based on water- and air-saturated digital rocks with different fractures. The ETC results were analyzed for the effect of saturated fluid and fracture parameters. Then, we used partial least squares (PLS) regression analysis to evaluate the relationship between ETC and the related parameters, including fracture length and aperture, angle between the fracture and the heat flux direction, porosity, and fluid thermal conductivity.

## 2. Model and Method

### 2.1. Thermal Conduction Model

The temperature gradient within an object leads to molecule collision and energy transfer, which is the process that defines thermal conduction. At the steady state, the thermal conduction of a homogeneous material can be described by Fourier's law [42]:

$$\vec{\varphi} = -\lambda \nabla T \quad (1)$$

where  $\varphi$  is the heat flux,  $\lambda$  is the thermal conductivity, and  $\nabla T$  is the temperature difference.

The thermal conduction model applied in this paper imposes a constant heat flux between the two opposing faces of the sample. The input and output temperatures are constant kept by a heating resistor and cooling tank. The remaining sample faces are thermally insulated planes. When the

temperature distribution of the sample is stable, the input and output heat fluxes are equal. Fourier's law of the whole sample is

$$\frac{\varphi_{\text{total}}}{S_{\text{in}}} = \lambda_e \frac{T_{\text{in}} - T_{\text{out}}}{L} \quad (2)$$

where  $\varphi_{\text{total}}$  is the total heat flux through the input surface ( $\text{W}/\text{m}^2$ );  $S_{\text{in}}$  is the area of the input surface ( $\text{m}^2$ );  $\lambda_e$  is the ETC of the sample ( $\text{W}/(\text{m} \cdot \text{K})$ );  $T_{\text{in}}$  and  $T_{\text{out}}$  are the input and output temperatures, respectively (K); and  $L$  is the length of the sample (m). The ETC is determined by the thermal conductivity of each phase in the sample.

Using this model, we performed thermal conduction simulations on digital rocks. In this study, the inlet and outlet temperatures were 273 K and 298 K. Therefore, we ignored the thermal conductivity changes in the matrix and pores due to the temperature increasing. We considered air and water as the fluid phases to estimate the ETC. The thermal conductivities of air and water were assumed as 0.026 and 0.6  $\text{W}/(\text{m} \cdot \text{K})$ , respectively. For the matrix, we assumed a thermal conductivity of 7.4  $\text{W}/(\text{m} \cdot \text{K})$  [43,44].

## 2.2. Reconstructed Digital Rocks with Different Fractures

The digital rocks with different fractures used in this paper were reconstructed from 2D thin section images adding fractures with different lengths, apertures, and angles. Figure 1 shows a schematic of how digital rocks with different fractures were obtained [45]. Firstly, based on 2D thin section images, we reconstructed the digital rocks (original system, Figure 1a) by the Markov chain Monte Carlo (MCMC) method [46,47]. To improve the simulation efficiency, we extracted a certain number of pixels randomly from the original system to get a small digital rock (random system, Figure 1b). The different fracture parameters were defined in the fracture system (Figure 1c), which had the same size with the random system so that the fracture could be added into the digital rock easily. After that, we integrated the random system and the fracture system together, and then the digital rocks with different fractures (final system, Figure 1d) could be used in the thermal conduction simulation directly.

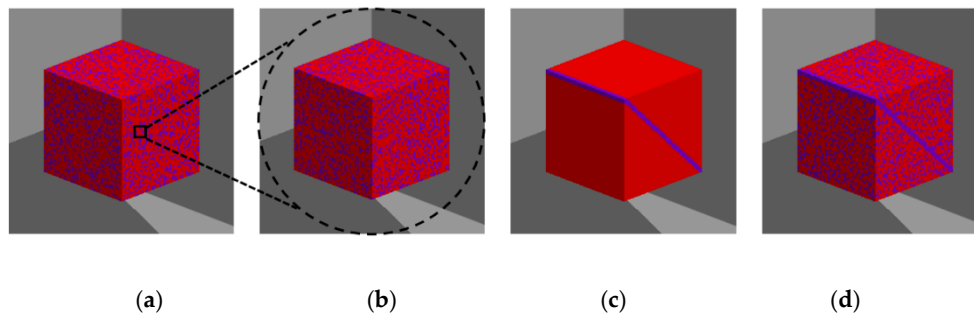


**Figure 1.** The reconstruction of digital rocks with different fractures: (a) original system; (b) random system; (c) fracture system; and (d) final system.

In this paper, the random system ( $50 \times 50 \times 50$  voxels) is shown in Figure 2a,b. The pore structure parameters of this digital rock in Table 1 were obtained by pore network model [47,48]. The ETCs along the X, Y, and Z directions were 2.64, 2.63, and 2.63  $\text{W}/(\text{m} \cdot \text{K})$ , respectively. Figure 2c to Figure 2e show the temperature distributions of three directions. We note that the ETCs from three orthogonal directions are almost the same; in this case, we inferred the random system to be isotropic. We obtained the fractured samples by adding fractures into this isotropic digital rock (every sample having one fracture), resulting in fracture angles of  $0^\circ$ ,  $30^\circ$ , and  $45^\circ$ ; lengths from 5 pixels to 50 pixels; and apertures from 2 pixels to 5 pixels, as shown in Figure 3.

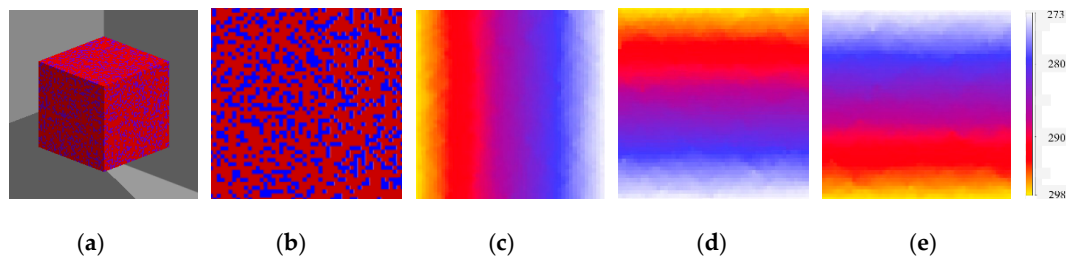


**Figure 2.** The extracted digital rock and the temperature distribution along three orthogonal heat flux directions: (a) The extracted digital rock of which the pore space is blue and the matrix is red. (b) The *xy* plane slice of extracted digital rock. The temperature distribution in (c) the *xy* plane with conduction along the X direction, (d) the *xy* plane with conduction along the Y direction, and (e) the *xz* plane with conduction along the Z direction.

**Table 1.** The parameters of the extracted digital rock.

Parameter	Value
Porosity (%)	31.43
Effective porosity (%)	31.40
Average pore radius ( $\mu\text{m}$ )	6.42
Average throat length ( $\mu\text{m}$ )	191
Average coordination number	7.23
Average tortuosity	4.24

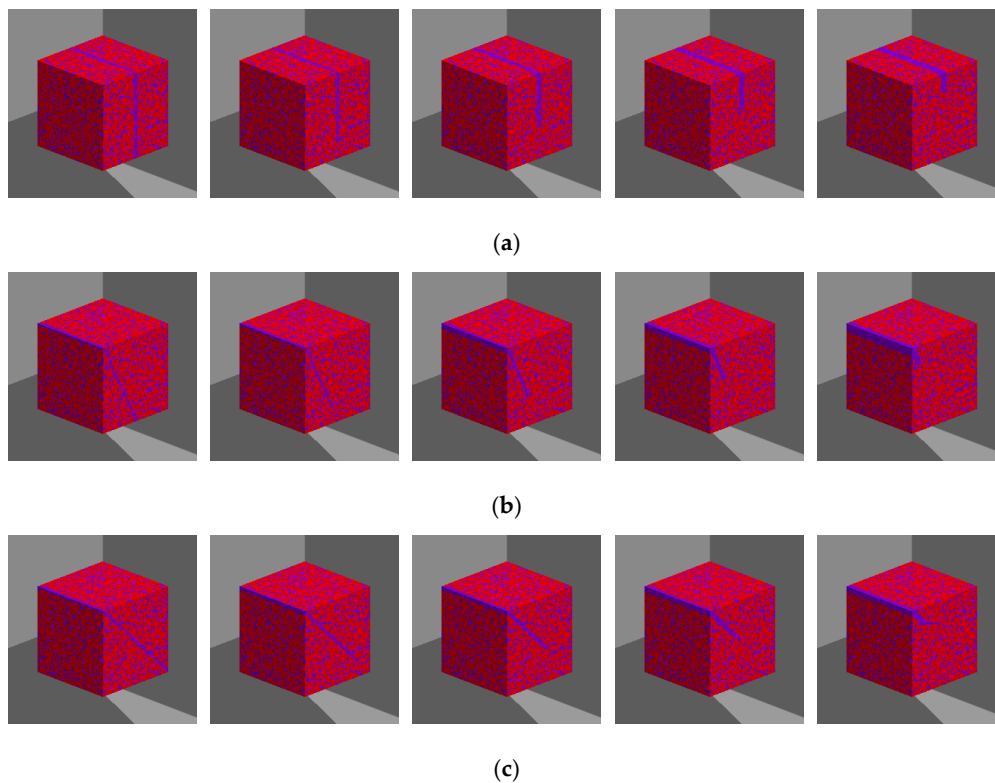


**Figure 3.** Digital rocks with different fracture parameters. Digital rocks with (a) vertical fracture and tilted fractures at (b) 30° and (c) 45°. The vertical length of each fracture is from 5 pixels to 50 pixels and the aperture is from 2 pixels to 5 pixels.

### 2.3. Partial Least Squares (PLS) Regression Analysis Method

When analyzing the relationship of multiple correlated variables, it is necessary to study the contribution of each independent variable to the dependent variables and better to obtain an accurate

predictive equation. In addition to multiple linear regression analysis (MLR) based on the classical least squares criterion, the partial least squares (PLS) regression method has been developed in recent years [49,50]. PLS regression provides a many-to-many linear regression model, especially when the number of variables with multiple correlations is large. The PLS regression method can relate different independent variables to describe the dependent variables by normalizing and combining features from principal component analysis and multiple regression [51,52].

We simply introduce the PLS modeling procedure of the dependent variables  $(y_1, y_2, \dots, y_p)$  and the independent variables  $(x_1, x_2, \dots, x_p)$ . From the independent and dependent variables, we extract the first components  $t_1$  and  $u_1$ , which are the linear combinations of  $(x_1, x_2, \dots, x_p)$  and  $(y_1, y_2, \dots, y_p)$ , respectively, with the most variation in information, to ensure that  $u_1$  has the largest correlation with  $t_1$ . Then, we set up the regression between the dependent variables  $(y_1, y_2, \dots, y_p)$  and  $t_1$  until we obtain the expected accuracy. Then, the partial least squares regression equation can be obtained. The detailed modeling procedures can be seen in [53,54].

### 3. Thermal Conduction Simulation on Reconstructed Digital Rocks

#### 3.1. Temperature Distribution in Digital Rocks with Different Fractures

We simulated thermal conduction to evaluate the effect of the fracture parameters (length, aperture, and angle) on the ETC. The digital rocks and their corresponding temperature distributions are shown in Figure 4, Figure 5, and Figure 6 when the saturated fluid is air. From Figure 4c, Figure 5c, and Figure 6c, we note that the temperature distribution is separated by the fractures. With incremented fracture length, the thermal conduction is obstructed by the fractures gradually. As the difference between the solid and fluid thermal conductivities is significant, compared to the matrix, the pore space is almost not conductive [55]. Therefore, the fractures can disturb the temperature field in an obvious way, especially when the fracture with a large length and aperture is vertical to the heat flux direction.

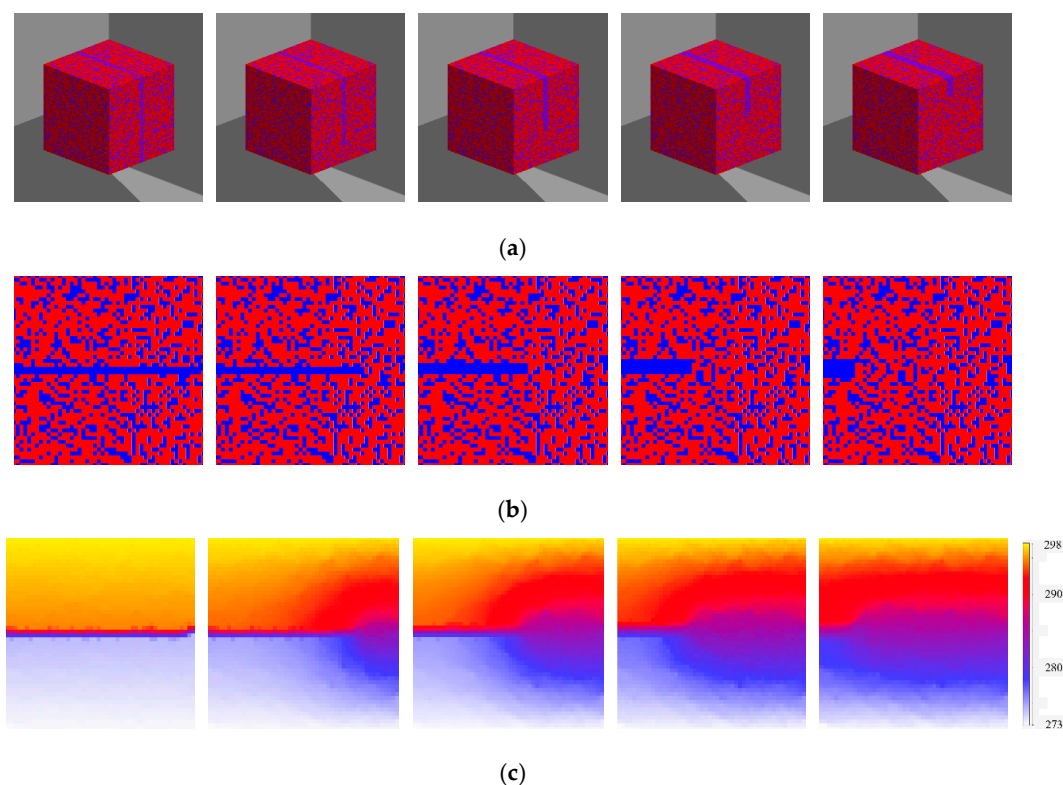


**Figure 4.** Digital rocks with vertical fractures: (a) digital rocks, (b) 2D slices, and (c) temperature distribution.

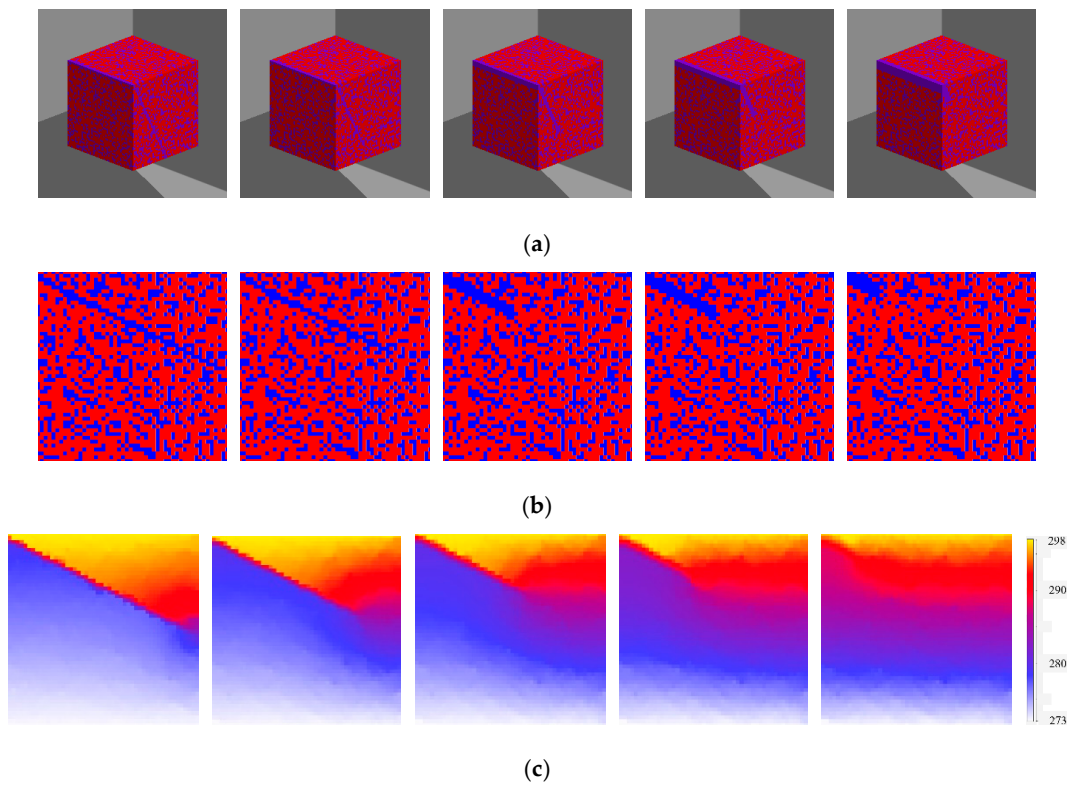


**Figure 5.** Digital rocks with tilted fractures ( $30^\circ$ ): (a) digital rocks, (b) 2D slices, and (c) temperature distribution.

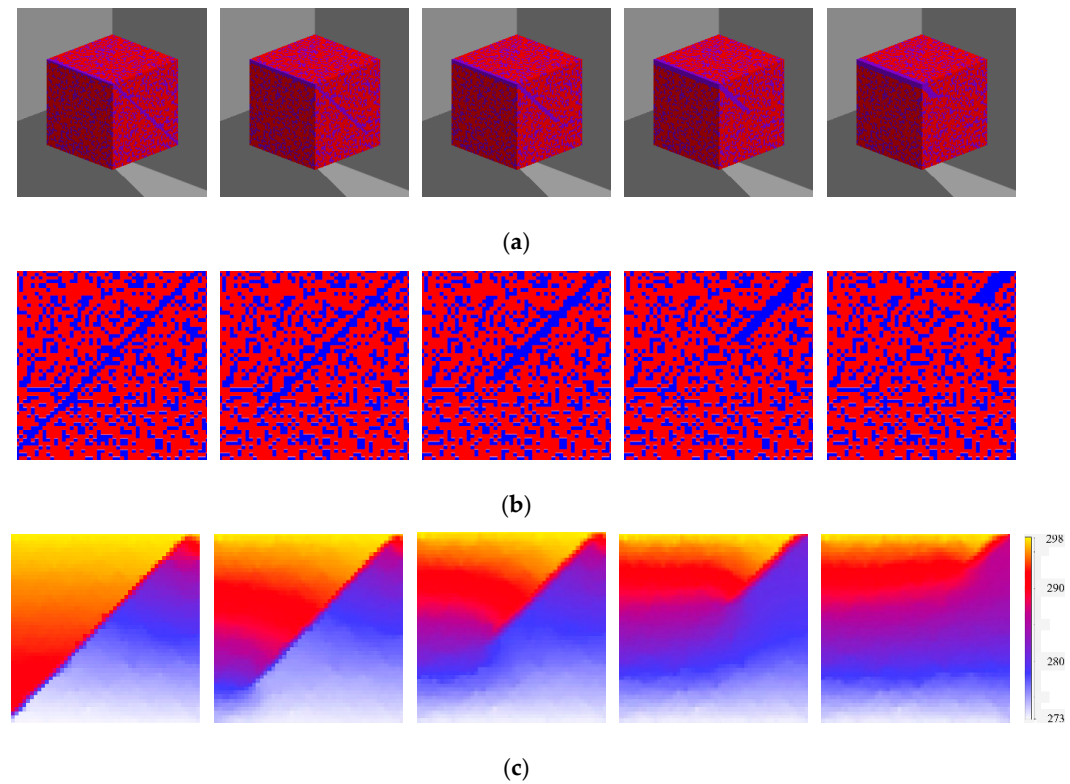


**Figure 6.** Digital rocks with tilted fractures ( $45^\circ$ ): (a) digital rocks, (b) 2D slices, and (c) temperature distribution.

### 3.2. ETC with Variable Saturated Fluid and Fracture Parameters

In order to study thermal anisotropy due to fractures, we calculated ETCs along the X, Y, and Z directions. In this paper, the “angle” refers to the angle between the fracture and the heat flux direction. Figure 7 shows how the ETC varies at different angles with respect to the fracture length and aperture under air and water saturation. It is obvious that the ETC reduction in air-saturated rocks is more apparent than that in water-saturated rocks with increasing fracture length, as shown in Figure 7. In this study, the thermal conductivity ratios of the solid to water and air were 12.34 and 284.62, respectively. A previous study [55] reported that fluid thermal conduction could cross pores effectively in porous media when the solid to fluid thermal conductivity ratio was less than 50. Therefore, when the fluid is conductive (water saturated), the fracture’s negative effect on ETC is less than that under nonconductive conditions (air saturated). Due to the significant difference between the solid and fluid, the thermal conduction mainly depends on the solid [11].

For a given angle and aperture, we note the reduction of ETC with increasing fracture length, as shown in Figure 7. However, the reduction degree is different at different ranges of length, causing the decrease to be nonlinear. When the fracture length is less than 5 pixels, the slightly reduced ETC is close to its initial value (for a digital rock without fracture, the fracture length is considered as 0 pixels). For the length range of 5 pixels to 15 pixels, we can observe the decrease of ETC reduction gradient clearly. As the fracture length increases continuously, a linear relationship between ETC and fracture length can be noted. A sharp reduction of ETC occurs when the fracture nearly or completely go through the digital rock at 45° (Figure 7c) and 90° (Figure 7e).

For the angle effect, when the heat flux is parallel to the fracture direction (Figure 7a), at the same fracture length, the effect degree of different fracture apertures is almost consistent. Due to a slight reduction in ETC, we note that the obstructive effect of the fracture can almost be ignored when the fracture is parallel to the heat flux. Whereas with increasing angle, the fracture length affects the ETC primarily [21]. When the direction of heat flux is vertical to the fracture (Figure 7e), as the length increases, the fracture obstruct the heat greatly, especially from 45 pixels to 50 pixels. Besides, for water-saturated conditions, due to the aperture increasing, the reduction gradient of ETC is almost the same. When air-saturated conditions, different apertures result in different reduction degrees of ETC. We note that the difference is significant between 2 pixels and 3 pixels when the angle is 30° (Figure 7b) and 60° (Figure 7d). For 45° (Figure 7c), a sharper decrease is observed at the aperture size of 3 pixels. However, when the aperture is 4 pixels or 5 pixels, the ETC difference is not obvious. Comparing the three fracture parameters, we note that the effect of the aperture on ETC is not as important as that of the fracture length and angle.

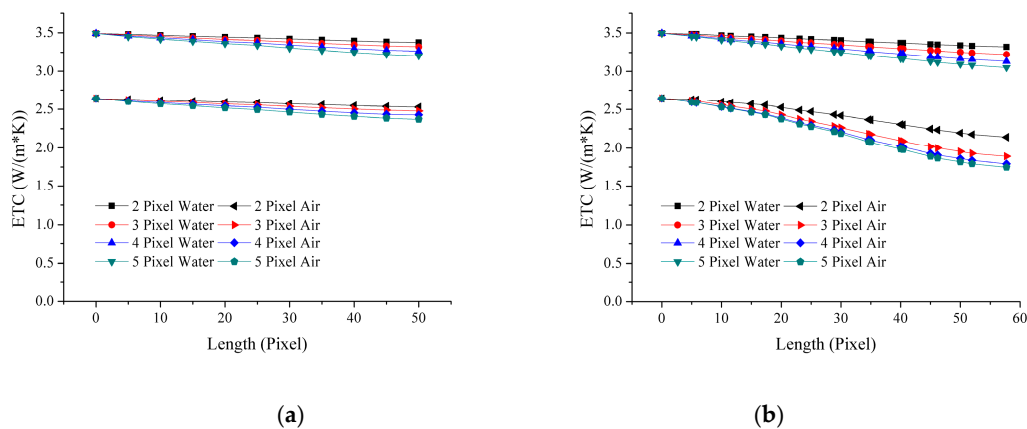
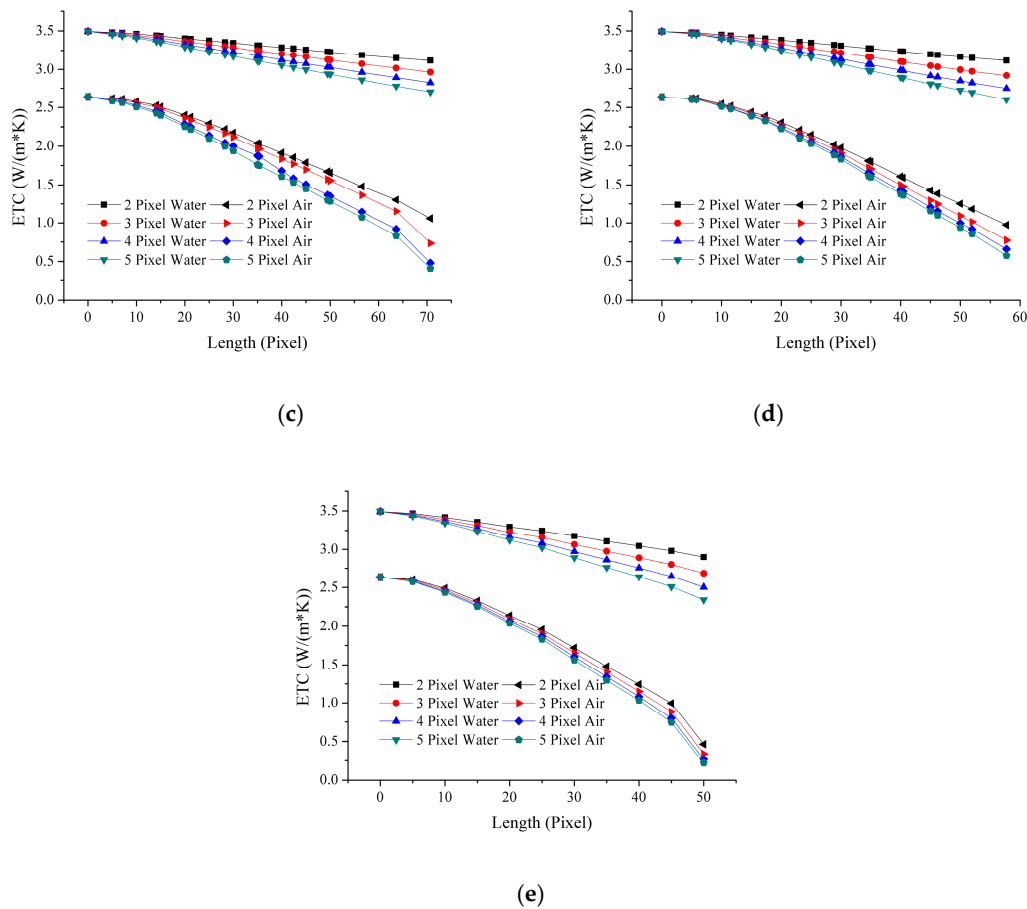


Figure 7. Cont.



**Figure 7.** Effective thermal conductivity as a function of fracture length and aperture. The angles between thermal conduction and the fracture were (a)  $0^\circ$ , (b)  $30^\circ$ , (c)  $45^\circ$ , (d)  $60^\circ$ , and (e)  $90^\circ$ .

#### 4. Partial Least Squares Regression Analysis

According to the discussion above, ETC decreases with increasing fracture length, fracture aperture, and angle. In addition, the thermal conductivity of the fluid also affects the ETC. However, these parameters have different influence degrees on ETC. It is challenging to describe the relationship between ETC and these parameters. Therefore, we used the partial least squares (PLS) regression method to quantify the correlation between ETC and these parameters. We set the fracture length and aperture, the angle between the heat flux and fracture direction, and the thermal conductivity of the fluid as the independent variables. The porosity is a necessary parameter when describing rock properties, and studies on the influence of porosity on ETC have been reported widely [56]. Therefore, we also considered the effect of porosity on ETC and set it as an independent variable. The ETC of digital rock is the dependent variable.

Using PLS regression analysis, we obtained the coefficients of the normalized regression equation and plotted them in Figure 8 to compare the contributions of the parameters to ETC obtained from the simulation results. We note that the fluid thermal conductivity is the only positive influencing factor of ETC, while the others have negative effects. As the digital rocks are only set to be air and water saturated, the fluid thermal conductivity has a strong influence on the ETC prediction. Except for the fluid effect, we note that the length and angle of the fracture are the most important factors contributing to the ETC, whereas the contribution of the aperture is negligible. In previous studies, the fracture parameters discussed in ETC studies were mainly the length and aperture [11]. From Figure 8, we note that the angle between the heat flux and fracture direction is an important parameter influencing ETC.

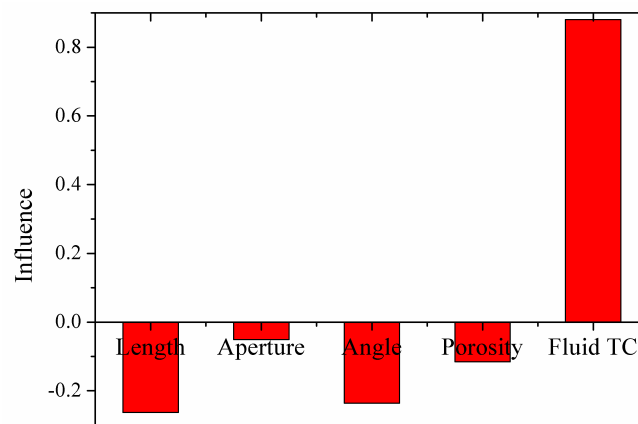


**Figure 8.** The influence degrees of parameters in effective thermal conductivity (ETC) prediction from partial least squares (PLS) analysis.

Based on the discussion in Chapter 3, we note the nonlinear relationship between the independent and dependent variables. Because PLS regression is a linear regression method, we plotted the ETC into the exponential coordinate system and then performed the PLS regression. The dimensionless fitting equation of ETC we obtained is

$$e^{\lambda_e} = 40.9908 - 7.4505 \cdot L_f/L_D - 22.0373 \cdot b_f/L_D - 4.3717 \cdot \theta\pi/180 - 69.4072 \cdot \phi + 29.6405 \cdot \lambda_f \quad (3)$$

where  $\lambda_e$  is the effective thermal conductivity ( $W/(m \cdot K)$ );  $L_f$  is the fracture length in pixels;  $L_D$  is the digital rock length in pixels;  $b_f$  is the fracture aperture in pixels;  $\theta$  is the direction angle between the heat flux and fracture;  $\phi$  is the porosity of the digital rock; and  $\lambda_f$  is the thermal conductivity of the saturated fluid ( $W/(m \cdot K)$ ).

To evaluate the accuracy degree of Equation (3), we plotted the predictive and actual ETCs together in the X and Y direction, respectively (Figure 9). When the scattered points are closer to the linear curve  $y = x$ , the accuracy of Equation (3) is better. We note that the fitting degree of the scattered points and linear curve is 0.97, from which we conclude that the fitting equation is very suitable.

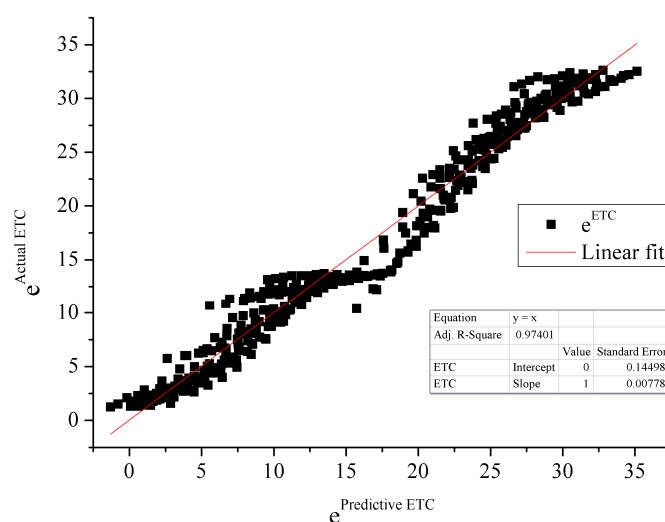


**Figure 9.** The fitting curve of the predictive ETC versus the actual ETC.

## 5. Conclusions

To evaluate the effect of fractures and saturated fluids on ETC, we simulated thermal conduction along three orthogonal ( $X$ ,  $Y$ , and  $Z$ ) directions under air- and water-saturated conditions on reconstructed digital rocks with different fractures. We drew the following conclusions:

(1) In thermal conduction on digital rocks with different fractures, the temperature distribution is separated by the fractures. The significant difference between the thermal conductivities of solid and fluid is the primary reason for the temperature distribution, and the thermal conduction mainly depends on the solid. As water has a higher thermal conductivity, the water-saturated digital rock is more thermally conductive, and the fracture's negative effect on ETC is less significant than that under air-saturated conditions.

(2) Nonlinear reduction of ETC is noted with increasing fracture length and angle. At larger length and angle, the smaller ETC is observed, while the effect of fracture aperture is not as important as that of the fracture length and angle.

(3) Based on PLS regression analysis, the fluid thermal conductivity is the only positive and the greatest influencing factor of ETC, while other factors have negative effects. The length and angle of the fracture are the significant influencing factors on ETC, while the impact of aperture can almost be ignored.

(4) A convincing prediction equation of ETC which considers related parameters of fractured digital rocks, including the fracture length and aperture, angle between the fracture and the heat flux direction, porosity, and the saturated fluid's thermal conductivity, is obtained based on the PLS regression method.

**Author Contributions:** Conceptualization, H.Y. and Y.Y.; methodology, H.Y. and L.Z. (Li Zhang); formal analysis, H.Y.; investigation, R.L.; resources, X.W.; writing—original draft preparation, H.Y.; writing—review and editing, R.A.; supervision, H.Y. and Y.Y.; funding acquisition, L.Z. (Li Zhang), R.L., X.W., Y.Y., L.Z. (Lei Zhang) and K.Z.

**Acknowledgments:** We acknowledge the following for their financial support: the National Natural Science Foundation of China (No. 51674280, 51490654, 51722406, 61573018), Key Research and Development Plan of Shandong Province (2018GSF116009), the Fundamental Research Funds for the Central Universities (No. 17CX05003, No. 18CX02031A), Shandong Provincial Natural Science Foundation (ZR2019JQ21), the Natural Science Foundation of Shan Dong Province (JQ201808), and Program for Changjiang Scholars and Innovative Research Team in University (IRT\_16R69).

**Conflicts of Interest:** The authors declare that there is no conflict of interest.

## References

1. Yao, J.; Zhang, X.; Sun, Z. Numerical simulation of the heat extraction in 3D-EGS with thermal-hydraulic-mechanical coupling method based on discrete fractures mode. *Geothermics* **2018**, *74*, 19–34. [[CrossRef](#)]
2. Sun, Z.X.; Zhang, X.; Xu, Y.; Yao, J.; Wang, H.X.; Lv, S.H.; Sun, Z.L.; Huang, Y.; Cai, M.Y.; Huang, X.X. Numerical simulation of the heat extraction in EGS with thermal-hydraulic-mechanical coupling method based on discrete fractures model. *Energy* **2017**, *120*, 20–33. [[CrossRef](#)]
3. Wang, T.; Sun, Z.; Zhang, K.; Jiang, C.; Xin, Y.; Mao, Q. Investigation on heat extraction performance of fractured geothermal reservoir using coupled thermal-hydraulic-mechanical model based on equivalent continuum Method. *Energies* **2019**, *12*, 127. [[CrossRef](#)]
4. Sun, Z.; Xin, Y.; Yao, J.; Zhang, K.; Zhuang, L.; Zhu, X.; Wang, T.; Jiang, C. Numerical investigation on the heat extraction capacity of dual horizontal wells in enhanced geothermal systems based on the 3D THM model. *Energies* **2018**, *11*, 280. [[CrossRef](#)]
5. Zuo, J.P.; Wang, J.T.; Sun, Y.J.; Chen, Y.; Jiang, G.H.; Li, Y.H. Effects of thermal treatment on fracture characteristics of granite from Beishan, a possible high-level radioactive waste disposal site in China. *Eng. Fract. Mech.* **2017**, *182*, 425–437. [[CrossRef](#)]
6. Chen, S.; Yang, C.; Wang, G. Evolution of thermal damage and permeability of Beishan granite. *Appl. Therm. Eng.* **2017**, *110*, 1533–1542. [[CrossRef](#)]

7. Zhu, G.P.; Yao, J.; Sun, H.; Zhang, M.; Xie, M.J.; Sun, Z.X.; Lu, T. The numerical simulation of thermal recovery based on hydraulic fracture heating technology in shale gas reservoir. *J. Nat. Gas Sci. Eng.* **2016**, *28*, 305–316. [[CrossRef](#)]
8. Ezeuko, C.C.; Gates, I.D. Thermal oil recovery from fractured reservoirs: Energy and emissions intensities. *Energy* **2018**, *155*, 29–34. [[CrossRef](#)]
9. Huai, X.L.; Wang, W.W.; Li, Z.G. Analysis of the effective thermal conductivity of fractal porous media. *Appl. Therm. Eng.* **2007**, *27*, 2815–2821. [[CrossRef](#)]
10. Pia, G.; Sanna, U. Case studies on the influence of microstructure voids on thermal conductivity in fractal porous media. *Case Stud. Therm. Eng.* **2014**, *2*, 8–13. [[CrossRef](#)]
11. Miao, T.J.; Cheng, S.J.; Chen, A.M.; Yu, B.M. Analysis of axial thermal conductivity of dual-porosity fractal porous media with random fractures. *Int. J. Heat Mass Transf.* **2016**, *102*, 884–890. [[CrossRef](#)]
12. Ramazanov, A.E.; Emirov, S.N. Baric and temperature dependences for the thermal conductivity of sedimentary rocks. *Bull. Russ. Acad. Sci. Phys.* **2012**, *76*, 1152–1156. [[CrossRef](#)]
13. Sun, Q.; Lv, C.; Cao, L.W.; Li, W.C.; Geng, J.S.; Zhang, W.Q. Thermal properties of sandstone after treatment at high temperature. *Int. J. Rock Mech. Min. Sci.* **2016**, *85*, 60–66. [[CrossRef](#)]
14. Abdulagatova, Z.; Abdulagatov, I.M.; Emirov, V.N. Effect of temperature and pressure on the thermal conductivity of sandstone. *Int. J. Rock Mech. Min. Sci.* **2009**, *46*, 1055–1071. [[CrossRef](#)]
15. Askari, R.; Hejazi, S.H.; Sahimi, M. Effect of deformation on the thermal conductivity of granular porous media with rough grain surface. *Geophys. Res. Lett.* **2017**, *44*, 8285–8293. [[CrossRef](#)]
16. Alishaev, M.G.; Abdulagatov, I.M.; Abdulagatova, Z.Z. Effective thermal conductivity of fluid-saturated rocks Experiment and modeling. *Eng. Geol.* **2012**, *135*, 24–39. [[CrossRef](#)]
17. Qin, X.; Cai, J.C.; Xu, P.; Dai, S.; Gan, Q. A fractal model of effective thermal conductivity for porous media with various liquid saturation. *Int. J. Heat Mass Transf.* **2019**, *128*, 1149–1156. [[CrossRef](#)]
18. Chen, Y.F.; Li, D.Q.; Jiang, Q.H.; Zhou, C.B. Micromechanical analysis of anisotropic damage and its influence on effective thermal conductivity in brittle rocks. *Int. J. Rock Mech. Min. Sci.* **2012**, *50*, 102–116. [[CrossRef](#)]
19. Ferone, C.; Colangelo, F.; Frattini, D.; Roviello, G.; Cioffi, R.; Maggio, R. Finite element method modeling of sensible heat thermal energy storage with innovative concretes and comparative analysis with literature benchmarks. *Energies* **2014**, *7*, 5291–5316. [[CrossRef](#)]
20. Hua, Y.; Zhao, T.; Guo, Z. Transient thermal conduction optimization for solid sensible heat thermal energy storage modules by the Monte Carlo method. *Energy* **2017**, *133*, 338–347. [[CrossRef](#)]
21. Zhou, H.; Liu, H.T.; Hu, D.W.; Zhang, F.; Yang, F.J.; Lu, J.J. Estimation of the effective thermal properties of cracked rocks. *Eur. J. Environ. Civ. Eng.* **2016**, *20*, 954–970. [[CrossRef](#)]
22. Choo, J.; Kim, Y.J.; Lee, J.H.; Yun, T.S.; Lee, J.; Kim, Y.S. Stress-induced evolution of anisotropic thermal conductivity of dry granular materials. *Acta Geotech.* **2012**, *8*, 91–106. [[CrossRef](#)]
23. Askari, R.; Hejazi, S.H.; Sahimi, M. Thermal Conduction in Deforming Isotropic and Anisotropic Granular Porous Media with Rough Grain Surface. *Transp. Porous Media* **2018**, *124*, 221–236. [[CrossRef](#)]
24. Andrä, H.; Combaret, N.; Dvorkin, J.; Glatt, E.; Han, J.; Kabel, M.; Keehm, Y.; Krzikalla, F.; Lee, M.; Madonna, C. Digital rock physics benchmarks—Part I: Imaging and segmentation. *Comput. Geosci.* **2013**, *50*, 25–32. [[CrossRef](#)]
25. Andrä, H.; Combaret, N.; Dvorkin, J.; Glatt, E.; Han, J.; Kabel, M.; Keehm, Y.; Krzikalla, F.; Lee, M.; Madonna, C. Digital rock physics benchmarks—Part II: Computing effective properties. *Comput. Geosci.* **2013**, *50*, 33–43. [[CrossRef](#)]
26. Song, R.; Liu, J.J.; Cui, M.M. A new method to reconstruct structured mesh model from micro computed tomography images of porous media and its application. *Int. J. Heat Mass Transf.* **2017**, *109*, 705–715. [[CrossRef](#)]
27. Zhang, Y.H.; Xu, X.M.; Lebedev, M.; Sarmadivaleh, M.; Barifcani, A.; Iglauer, S. Multi-scale X-ray computed tomography analysis of coal microstructure and permeability changes as a function of effective stress. *Int. J. Coal Geol.* **2016**, *165*, 149–156. [[CrossRef](#)]
28. Yang, Y.F.; Yao, J.; Wang, C.C.; Gao, Y.; Zhang, Q.; An, S.Y.; Song, W.H. New pore space characterization method of shale matrix formation by considering organic and inorganic pores. *J. Nat. Gas Sci. Eng.* **2015**, *27*, 496–503. [[CrossRef](#)]

29. An, S.Y.; Yao, J.; Yang, Y.F.; Zhang, L.; Zhao, J.L.; Gao, Y. Influence of pore structure parameters on flow characteristics based on a digital rock and the pore network model. *J. Nat. Gas Sci. Eng.* **2016**, *31*, 156–163. [[CrossRef](#)]
30. Song, W.H.; Yao, J.; Li, Y.; Sun, H.; Zhang, L.; Yang, Y.F.; Zhao, J.L.; Sui, H.G. Apparent gas permeability in an organic-rich shale reservoir. *Fuel* **2016**, *181*, 973–984. [[CrossRef](#)]
31. Zhao, J.L.; Yao, J.; Zhang, M.; Zhang, L.; Yang, Y.F.; Sun, H.; An, S.Y.; Li, A.F. Study of gas flow characteristics in tight porous media with a microscale Lattice Boltzmann model. *Sci. Rep.* **2016**, *6*, 32393. [[CrossRef](#)]
32. Sun, H.; Yao, J.; Cao, Y.C.; Fan, D.Y.; Zhang, L. Characterization of gas transport behaviors in shale gas and tight gas reservoirs by digital rock analysis. *Int. J. Heat Mass Transf.* **2017**, *104*, 227–239. [[CrossRef](#)]
33. Yang, Y.F.; Liu, Z.H.; Sun, Z.X.; An, S.Y.; Zhang, W.J.; Liu, P.F.; Yao, J.; Ma, J.S. Research on stress sensitivity of fractured carbonate reservoirs based on CT technology. *Energies* **2017**, *10*, 1833. [[CrossRef](#)]
34. Zhang, K.; Ma, X.P.; Li, Y.L.; Wu, H.Y.; Cui, C.Y.; Zhang, X.M.; Zhang, H.; Yao, J. Parameter prediction of hydraulic fracture for tight reservoir based on micro-seismic and history matching. *Fractals* **2018**, *26*, 1840009. [[CrossRef](#)]
35. Zhang, L.; Cui, C.; Ma, X.; Sun, Z.; Liu, F.; Zhang, K. A fractal discrete fracture network model for history matching of naturally fractured reservoirs. *Fractals* **2019**, *27*, 1940008. [[CrossRef](#)]
36. Zhou, H.; Zhou, M.X.; Cheng, M.; Guo, X.T.; Li, Y.W.; Ma, P.N.; Cen, K.F. High resolution X-ray microtomography for the characterization of pore structure and effective thermal conductivity of iron ore sinter. *Appl. Therm. Eng.* **2017**, *127*, 508–516. [[CrossRef](#)]
37. Fan, L.F.; Gao, J.W.; Wu, Z.J.; Yang, S.Q.; Ma, G.W. An investigation of thermal effects on micro-properties of granite by X-ray CT technique. *Appl. Therm. Eng.* **2018**, *140*, 505–519. [[CrossRef](#)]
38. Zhao, J.L.; Kang, Q.J.; Yao, J.; Zhang, L.; Li, Z.; Yang, Y.F.; Sun, H. Lattice Boltzmann simulation of liquid flow in nanoporous media. *Int. J. Heat Mass Transf.* **2018**, *125*, 1131–1143. [[CrossRef](#)]
39. Rostami, A.; Masoudi, M.; Ghaderi-Ardakani, A.; Arabloo, M.; Amani, M. Effective Thermal Conductivity Modeling of Sandstones: SVM Framework Analysis. *Int. J. Thermophys.* **2016**, *37*, 59. [[CrossRef](#)]
40. Vaferi, B.; Gitifar, V.; Darvishi, P.; Mowla, D. Modeling and analysis of effective thermal conductivity of sandstone at high pressure and temperature using optimal artificial neural networks. *J. Pet. Sci. Eng.* **2014**, *119*, 69–78. [[CrossRef](#)]
41. Oezbek, H. Thermal conductivity of multi-fluid saturated porous media. *J. Pet. Technol.* **1976**, *29*, 275.
42. Büttner, H.; Mokross, F. Fourier's law and thermal conduction. *Nature* **1984**, *311*, 217–218. [[CrossRef](#)]
43. Pribnow, D.; Williams, C.F.; Sass, J.H.; Keating, R. Thermal conductivity of water-saturated rocks from the KTB Pilot Hole at temperatures of 25 to 300 °C. *Geophys. Res. Lett.* **1996**, *23*, 391–394. [[CrossRef](#)]
44. Askari, R.; Taheri, S.; Hejazi, S.H. Thermal conductivity of granular porous media: A pore scale modeling approach. *AIP Adv.* **2015**, *5*, 455–460. [[CrossRef](#)]
45. Wang, X.; Yao, J.; Yang, Y.; Wang, C.; Pu, D. Permeability prediction in digital core with curved fractures based on combined plate model. *J. China Univ. Pet. Ed. Nat. Sci.* **2013**, *37*, 82–86.
46. Wu, K.J.; Dijke, M.I.J.V.; Couples, G.D.; Jiang, Z.Y.; Ma, J.S.; Sorbie, K.S.; Crawford, J.; Young, I.; Zhang, X.X. 3D stochastic modelling of heterogeneous porous media—applications to reservoir rocks. *Transp. Porous Media* **2006**, *65*, 443–467. [[CrossRef](#)]
47. Yang, Y.F.; Wang, K.; Zhang, L.; Sun, H.; Zhang, K.; Ma, J.S. Pore-scale simulation of shale oil flow based on pore network model. *Fuel* **2019**, *251*, 683–692. [[CrossRef](#)]
48. Yang, Y.F.; Yang, H.Y.; Tao, L.; Yao, J.; Wang, W.D.; Zhang, K.; Luquot, L. Microscopic determination of remaining oil distribution in sandstones with different permeability scales using computed tomography scanning. *J. Energy Resour. Technol.* **2019**, *141*, 092903. [[CrossRef](#)]
49. Tobias, R.D. An Introduction to Partial Least Squares Regression. In Proceedings of the Twentieth Annual SAS Users Group International Conference, Orlando, FL, USA, 2 April 1995; SAS Institute Inc.: Cary, NC, USA, 1995; pp. 1250–1257.
50. Mehmood, T.; Liland, K.H.; Snipen, L.; Sæbø, S. A review of variable selection methods in partial least squares regression. *Chemom. Intell. Lab. Syst.* **2012**, *118*, 62–69. [[CrossRef](#)]
51. Yang, Y.; Liu, Z.; Yao, J.; Zhang, L.; Ma, J.; Hejazi, S.; Luquot, L.; Ngarta, T. Flow simulation of artificially induced microfractures using digital rock and Lattice Boltzmann Methods. *Energies* **2018**, *11*, 2145. [[CrossRef](#)]
52. Liu, K.Q.; Ostadhassan, M.; Kong, L.Y. Multifractal characteristics of Longmaxi Shale pore structures by N-2 adsorption: A model comparison. *J. Pet. Sci. Eng.* **2018**, *168*, 330–341. [[CrossRef](#)]

53. Geladi, P.; Kowalski, B.R. Partial least-squares regression: A tutorial. *Anal. Chim. Acta* **1986**, *185*, 1–17. [[CrossRef](#)]
54. Wold, S.; Ruhe, A.; Wold, H.; Dunn, W.J., III. The collinearity problem in linear regression. The partial least squares (PLS) approach to generalized inverses. *Siam J. Sci. Stat. Comput.* **1984**, *5*, 735–743. [[CrossRef](#)]
55. Deng, Z.; Liu, X.; Huang, Y.; Zhang, C.; Chen, Y. Heat conduction in porous media characterized by fractal geometry. *Energies* **2017**, *10*, 1230. [[CrossRef](#)]
56. Haffen, S.; Géraud, Y.; Rosener, M.; Diraison, M. Thermal conductivity and porosity maps for different materials: A combined case study of granite and sandstone. *Geothermics* **2017**, *66*, 143–150. [[CrossRef](#)]



© 2019 by the authors. Licensee MDPI, Basel, Switzerland. This article is an open access article distributed under the terms and conditions of the Creative Commons Attribution (CC BY) license (<http://creativecommons.org/licenses/by/4.0/>).